The Astrophysical Journal, 983:22 (13pp), 2025 April 10 https://doi.org/10.3847/1538-4357/adb7df

Detection of Molecular Clouds in the PeVatron Candidate Source LHAASO J0341+5258 by the Nobeyama 45-m Radio Telescope

Naomi Tsuji[1,2,3], Shunya Takekawa[4], Kaya Mori[5], Alison Mitchell[6], Shuo Zhang[7], Priyadarshini Bangale[8], Stephen DiKerby[7], Tülün Ergin[7], Jooyun Woo[5], Samar Safi-Harb[9], and Shinta Kasuya[1]
[1] Faculty of Science, Kanagawa University, 3-27-1 Rokukakubashi, Kanagawa-ku, Yokohama, Kanagawa 221-8686, Japan
[2] Interdisciplinary Theoretical & Mathematical Science Program (iTHEMS), RIKEN, 2-1, Hirosawa, Saitama 351-0198, Japan
[3] Department of Physics, Rikkyo University, Nishi-Ikebukuro 3-34-1, Toshima-ku, Tokyo, 171-8501, Japan
[4] Department of Applied Physics, Faculty of Engineering, Kanagawa University, 3-27-1 Rokkakubashi, Kanagawa-ku, Yokohama, Kanagawa 221-8686, Japan
[5] Columbia Astrophysics Laboratory, Columbia University, 538 West 120th Street, New York, NY 10027, USA
[6] Erlangen Centre for Astroparticle Physics, Friedrich-Alexander-Universität Erlangen-Nürnberg, Nikolaus-Fiebiger-Str. 2, Erlangen 91058, Germany
[7] Department of Physics and Astronomy, Michigan State University, East Lansing, MI 48824, USA
[8] Department of physics, Temple University, Philadelphia, PA 19122, USA
[9] Department of Physics and Astronomy, University of Manitoba, Winnipeg, MB R3T 2N2, Canada
Received 2024 December 24; revised 2025 January 29; accepted 2025 February 2; published 2025 April 2

Abstract

We report a new CO observation survey of LHAASO J0341+5258, using the Nobeyama Radio Observatory 45-m telescope. LHAASO J0341+5258 is one of the unidentified ultra-high-energy (UHE; $E > 100$ TeV) gamma-ray sources detected by LHAASO. Our CO observations were conducted in 2024 February and March, with a total observation time of 36 hr, covering the LHAASO source ($\sim 0.^{\circ}3$–$0.^{\circ}5$ in radius) and its surrounding area ($1^{\circ} \times 1.^{\circ}5$). Within the LHAASO source extent, we identified five compact (<2 pc) molecular clouds at nearby distances (<1–4 kpc). These clouds can serve as proton–proton collision targets, producing hadronic gamma rays via neutral pion decays. Based on the hydrogen densities (700–5000 cm^{-3}) estimated from our CO observations and archived H I data from the Dominion Radio Astrophysical Observatory survey, we derive the total proton energy of W_p ($E > 1$ TeV) $\sim 10^{45}$ erg to account for the gamma-ray flux. One of the molecular clouds appears to be likely associated with an asymptotic giant branch (AGB) star with an extended CO tail, which may indicate some particle acceleration activities. However, the estimated maximum particle energy below 100 TeV makes the AGB-like star unlikely to be a PeVatron site. We conclude that the UHE emission observed in LHAASO J0341+5258 could be due to hadronic interactions between the newly discovered molecular clouds and TeV–PeV protons originating from a distant SNR or due to leptonic emission from a pulsar wind nebula candidate, which is reported in our companion X-ray observation paper.

Unified Astronomy Thesaurus concepts: Gamma-rays (637); Molecular clouds (1072); Cosmic rays (329)

1. Introduction

Cosmic rays (CRs), primarily high-energy protons, with energies below the *knee* of their spectrum—approximately a few PeV—have been proposed to originate from supernova remnants (SNRs) in our Galaxy. The so-called "pion bump" structure, which is a smoking gun for accelerated protons, has likely been identified in gamma-ray spectra of several SNRs (M. Ackermann et al. 2013). This discovery has led to SNRs being widely accepted as primary contributors to CR protons. However, there is a lack of decisive observational evidence as to whether SNRs are indeed capable of accelerating particles up to the knee, despite numerous dedicated studies (e.g., T. Tanaka et al. 2008; H.E.S.S. Collaboration et al. 2018; A. U. Abeysekara et al. 2020; N. Tsuji et al. 2021). In fact, the gamma-ray spectra of most SNRs have exponential cutoffs at TeV (S. Funk 2015), making it challenging to reconcile them with particle acceleration up to PeV. One possible resolution is that SNRs act as PeVatrons only for a short period early in their evolution.

Recently, (sub)PeV gamma-ray astronomy has begun, driven by the detection of ultra-high-energy (UHE; $E > 100$ TeV) gamma rays by air shower arrays, such as Tibet ASγ, HAWC, and LHAASO (M. Amenomori et al. 2005; LHAASO Collaboration 2010; HAWC Collaboration et al. 2020). The findings by these observatories may be on the verge of changing our understanding of the SNR paradigm (SNRs as primary CR accelerators), especially for CRs with PeV energies. Measurements of UHE gamma rays can help us pinpoint the locations of CRs with PeV energies and plausible accelerators of PeV CRs (i.e., PeVatrons) in the vicinity. More recently, stellar clusters and microquasars have emerged as new classes of PeVatrons, after some of them were detected in the UHE gamma-ray band (e.g., Z. Cao et al. 2021a; F. Aharonian et al. 2022; R. Alfaro et al. 2024; H.E.S.S. Collaboration 2024; LHAASO Collaboration 2024a, 2024b). On the other hand, the UHE emission in the W51 complex likely provides the first evidence of particle acceleration up to the PeV energy range in SNR W51C (Z. Cao et al. 2024b).

Nevertheless, there is still a non-negligible number of unidentified TeV–PeV gamma-ray sources. For example, about 40% of the 90 sources listed in the first LHAASO catalog (Z. Cao et al. 2024a) have no apparent associations and remain unidentified. Some of them remain unidentified simply due to a lack of observational data at other wavelengths. Radio and X-ray follow-up observations have already proved the importance of multiwavelength study, such as in HESS

Table 1
LHAASO Sources in the J0341 Region

Name	Instrument[a]	(ℓ, b)[b] (deg)	Size[c] (deg)	Γ	$TS_{>100\ TeV}$[d]	References
LHAASO J0341+5258	KM2A	(146.94, −1.792)	0.29 ± 0.06	2.98 ± 0.19	···	Z. Cao et al. (2021b)
1LHAASO J0339+5307	KM2A	(146.58, −1.861)	<0.22	3.64 ± 0.16	···	Z. Cao et al. (2024a)
	WCDA	···	···	···	···	Z. Cao et al. (2024a)
1LHAASO J0343+5254u	KM2A	(147.20, −1.676)	0.20 ± 0.02	3.53 ± 0.10	20.2	Z. Cao et al. (2024a)
	WCDA	(146.89, −1.728)	0.33 ± 0.05	1.70 ± 0.19	···	Z. Cao et al. (2024a)

Notes.
[a] The energy range of KM2A is >25 TeV, and that of WCDA is 1–25 TeV.
[b] The uncertainty on the position is $\sim 0.^{\circ}1$.
[c] The size indicates r_{39} (the 39% containment radius of the 2D Gaussian model), except that the 95% upper limit is provided for 1LHAASO J0339+5307.
[d] $TS_{>100\ TeV}$ is a test statistic value of detection above 100 TeV.

J1702−420 (L. Giunti et al. 2022) and LHAASO J2108+5157 (E. de la Fuente et al. 2023).

There exists a long-standing question about the nature of gamma-ray sources: leptonic (inverse-Compton scattering—ambient photons upscattered by accelerated electrons—or nonthermal bremsstrahlung) or hadronic (the decay of pions produced in interactions between accelerated protons and low-energy protons in ambient gas). Identifying gamma rays as hadronic emission is meaningful in the context of CRs, which predominantly consist of energetic protons. Hadronic gamma rays should be accompanied by dense gas, such as atomic and molecular clouds, which can be revealed by radio observations. Detecting neutrinos produced in the hadronic process would be another evidence of proton acceleration. Furthermore, in the hadronic scenario, the same proton–proton interactions produce charged pions, decaying into muons and secondary electrons and positrons. Thus, measuring the synchrotron radiation from these secondary electrons can be a strong indication for hadronic gamma rays, although it has not been detected yet (F. A. Aharonian 2013; N. Tsuji et al. 2024).

To advance our understanding of the PeVatron population, we need to investigate the unidentified UHE gamma-ray sources and reveal their origins one by one. In this paper, we focus on one of the PeVatron candidates and unidentified sources, LHAASO J0341+5258 (hereafter, J0341). This source was discovered by LHAASO's Kilometer Squared Array (KM2A) as an extended source, as summarized in Table 1 (Z. Cao et al. 2021b). In the following catalog (Z. Cao et al. 2024a), it was split into two sources: 1LHAASO J0339+5307 (only detected by KM2A) and 1LHAASO J0343+5254u (detected by both KM2A and the Water Cherenkov Detector Array (WCDA); see Table 1 and Figure 1 for details). Note that 1LHAASO J0343+5254u is detected in the UHE gamma-ray band. Although this region seems to be crowded with two or three LHAASO source components, the overall spectrum is hard ($\Gamma \approx 1.7$) in the 1–25 TeV energy range and becomes softened ($\Gamma \approx 3.5$) above 25 TeV, indicating the existence of a cutoff or curvature. Indeed, the spectrum in Z. Cao et al. (2021b) appeared to be better fit by a cutoff power-law or log-parabola model. Later, P. Bangale & X. Wang (2023) reported the gamma-ray detection at 10–200 TeV by HAWC and an upper limit at 0.5–50 TeV by VERITAS. Within the gamma-ray extent measured by LHAASO, there is an unidentified GeV gamma-ray-emission region, 4FGL J0340.4+5302, showing a curved spectrum with a peak energy around 200 MeV (S. Abdollahi et al. 2020; Z. Cao et al. 2021b). A. Kar & N. Gupta (2022) and A. De Sarkar & P. Majumdar (2024) conducted detailed modelings, inferring that the maximum CR energy would be roughly 200 TeV, either in leptonic or hadronic. Although there are three ROSAT X-ray point-like sources within the gamma-ray extension, there is no known extended X-ray emission so far. As part of an approved AO-22 XMM-Newton Large Program, the J0341 region was observed in 2024 February (Figure 1), and an associated publication is in preparation (S. DiKerby et al. 2025).

In this paper, we search for molecular clouds in the PeVatron candidate source J0341, using the Nobeyama Radio Observatory (NRO) 45-m radio telescope. We present an observation overview in Section 2 and the analysis and results in Section 3. We also report the results of analysis of the archival H I and radio continuum data in Section 4. The discussion and conclusions are described in Sections 5 and 6, respectively.

2. Observations

The $^{12}CO(J = 1–0)$, $^{13}CO(J = 1–0)$, and $C^{18}O(J = 1–0)$ data were obtained with the NRO 45 m radio telescope in 2024 February and March. We scanned an area of 1.5×1 deg^2, centered at $(\ell, b) = (146.^{\circ}7, -1.^{\circ}7)$, as shown in Figure 1. The scanning was made along the Galactic latitude, and the observations were performed in on-the-fly mapping mode (T. Sawada et al. 2008). The total observation time was 36 hr. The spatial resolution of the NRO 45-m telescope is 15″, which is much improved compared to the existing survey data (e.g., the CfA map with the angular resolution of $0.^{\circ}5$; T. M. Dame et al. 2001).

We made use of the four-beam receiver FOREST (T. Minamidani et al. 2016) and the autocorrelation spectrometer SAM45 (N. Kuno et al. 2011). The system noise temperatures including the atmosphere were between 300 and 400 K at 115 GHz. The bandwidth and resolution were 122.07 kHz both at 115 GHz and 110 GHz. The half-power beam width is 14″ at 115 GHz and 15″ at 110 GHz.[10] The observations were made by the 2:1 ON–OFF position switching mode. The OFF points were centered at $(\ell, b) = (148.^{\circ}5, -1.^{\circ}9)$ for $\ell \geqslant 146.^{\circ}5$ and $(\ell, b) = (143.^{\circ}7, -2.^{\circ}9)$ for $\ell \leqslant 146.^{\circ}5$. The pointing accuracy was checked every ∼2 hr by observing

[10] https://www.nro.nao.ac.jp/~nro45mrt/html/prop/eff/eff_latest.html

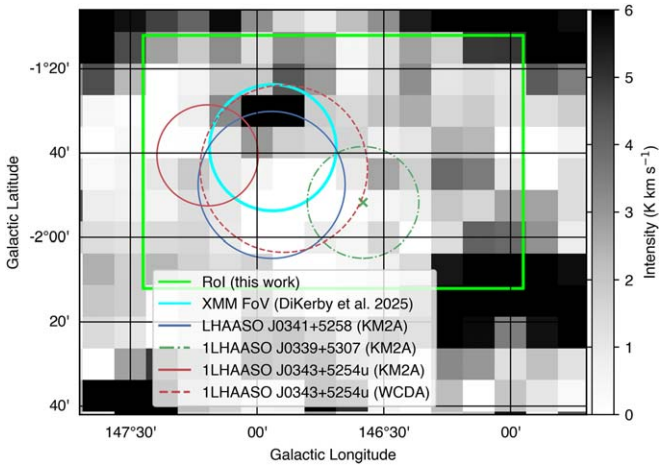

Figure 1. The CfA ^{12}CO($J = 1$–0) map (T. M. Dame et al. 2001; T. M. Dame & P. Thaddeus 2022), integrated from -40 to 10 km s^{-1}, in the J0341 region. The blue and red circles show the gamma-ray extents of J0341 and 1LHAASO J0343+5254u, respectively. For 1LHAASO J0339+5307, which was detected as a point-like source, the best-fit position and the 95% statistical upper limit of its radius are shown with the dark green cross and the dashed–dotted circle, respectively. The green rectangle indicates the region of 1.5 × 1 deg^2 that we scanned with the NRO 45-m telescope. The cyan circle shows the field of view of the XMM-Newton data (S. DiKerby et al. 2025).

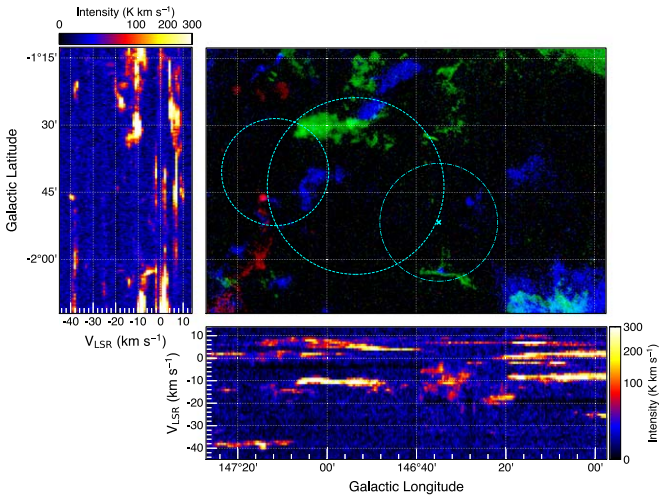

Figure 2. ^{12}CO($J = 1$–0) RGB image and position–velocity maps. In the RGB image, the red, green, and blue indicate the velocity-integrated maps at -41 to -37 km s^{-1}, -15 to -5 km s^{-1}, and -3 to 5 km s^{-1}, respectively. The cyan circles indicate the 1LHAASO sources (Z. Cao et al. 2024a), as summarized in Figure 1. In the Galactic latitude (longitude)–velocity map, the intensity is integrated over the entire region along the Galactic longitude (latitude).

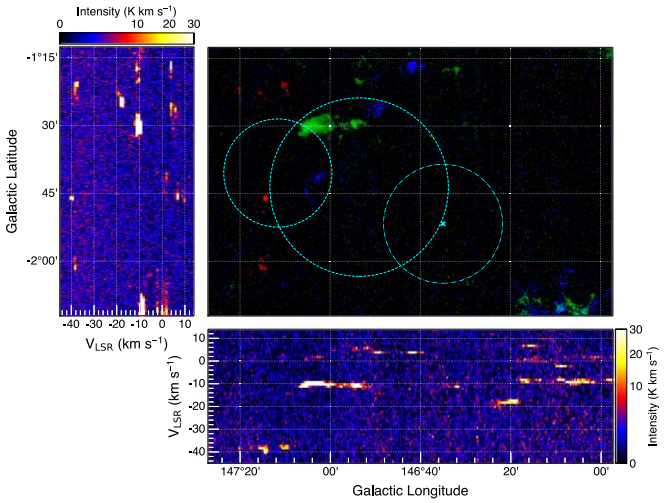

Figure 3. The same as Figure 2 but for ^{13}CO($J = 1$–0).

the SiO maser, S-per, at the position of $(\ell, b) = (134.^{\circ}62, -2.^{\circ}1949)$, using the H40 receiver. We checked that the pointing accuracy was better than 3″ in both azimuth and elevation. Calibration of the antenna temperature (T_a^*) was accomplished by the standard chopper-wheel method (M. L. Kutner & B. L. Ulich 1981).

All data were reduced using the NOSTAR reduction package. To determine and subtract the baseline, we conducted a linear fitting in ranges from -200 to -150 km s^{-1} and from 150 to 200 km s^{-1}. The antenna temperature (T_a^*) was converted to the main-beam temperature ($T_{\rm MB}$) by dividing by the main-beam efficiency ($\eta_{\rm MB}$), as $T_{\rm MB} = T_a^*/\eta_{\rm MB}$. The applied $\eta_{\rm MB}$, provided by the observatory (see footnote 10), was 0.35 at 115 GHz and 0.40 at 110 GHz. As an intensity calibration source, we observed a dense cloud region seen in Z. Cao et al. (2021a), which is characterized by a circle centered at $(\ell, b) = (147.^{\circ}05, -1.^{\circ}5098)$ and a radius of 1.′25. The flux of this calibration source was fairly constant (less than 10%) during the observation dates, thus we combined all the data at different epochs without scaling.

Maps were produced by convolution using Bessel–Gaussian functions. The spatial and velocity grids have sizes of 7.″5 and 1 km s^{-1}, respectively. The velocity coverage is from -150 to 150 km s^{-1}. The rms noise level in $T_{\rm MB}$ is 1.15 K and 0.324 K at 115 and 110 GHz, respectively. We applied a 3 rms cut to reduce the noise level for the following analyses.

3. Analysis and Results

Figure 2 shows the velocity-integrated and position–velocity maps of ^{12}CO($J = 1$–0), and Figure 3 shows those of ^{13}CO($J = 1$–0), obtained by the NRO 45 m telescope. Although the velocity coverage of our observations is from -150 to 150 km s^{-1}, there is no significant signal at $V_{\rm LSR} < -40$ km s^{-1} and $V_{\rm LSR} > 10$ km s^{-1}. As illustrated in Figures 2 and 3 (see also Figures 9 and 10 in Appendix A), there exist some clouds at different velocities in the region of interest (RoI), and we divide them into three groups: (1) -41 km s^{-1} $\leqslant V_{\rm LSR} < -37$ km s^{-1}; (2) -15 km s^{-1} $\leqslant V_{\rm LSR} < -5$ km s^{-1}; and (3) -3 km s^{-1} $\leqslant V_{\rm LSR} < 5$ km s^{-1}.

We found five molecular clouds within the gamma-ray-emitting region, referred to as Clouds A–E. Figure 4 shows a velocity-integrated map and spectrum extracted from each cloud. The position and the size are summarized in Table 2. We fit the velocity spectrum in Figure 4 with a Gaussian model and show the best-fit values (i.e., the Gaussian center $V_{\rm LSR}$ and FWHM $\Delta V_{\rm LSR}$) in Table 2.

The C^{18}O($J = 1$–0) data were also analyzed in the same way. However, we could not find significant emission, except for a tiny region centered at $(\ell, b) = (147.^{\circ}0736, -1.^{\circ}4945)$ with a radius of 1.′8 in the -13 to -8 km s^{-1} map. The peak and averaged intensities within the circle are 3.1 K and 0.76 K, respectively, which are 11 and 2.8 times greater than the average rms value of 0.27 K. This C^{18}O($J = 1$–0) emission is located inside Cloud C and likely represents the "core" of that dense cloud.

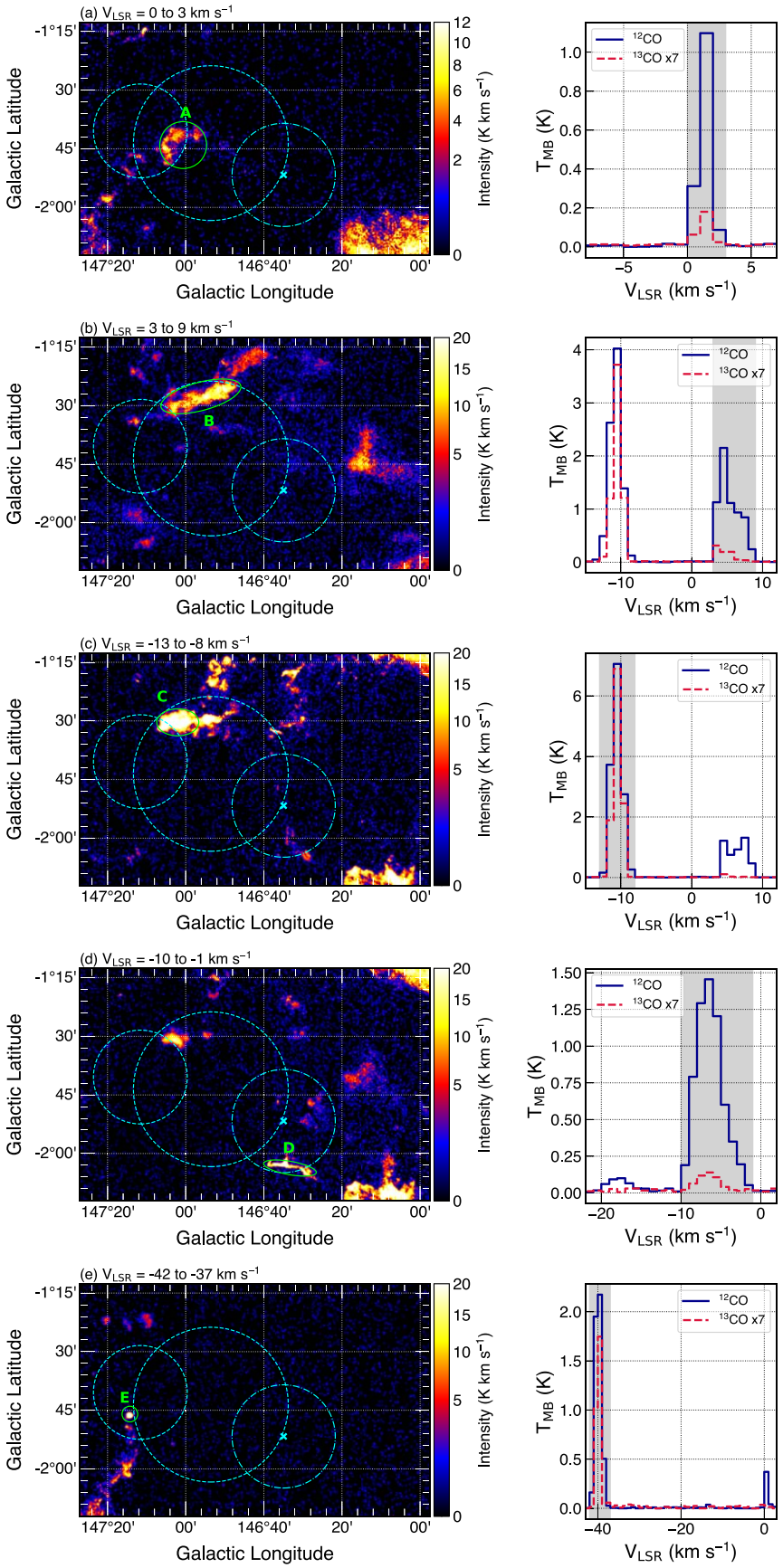

Figure 4. ^{12}CO($J = 1$–0) map (left) and spectrum (right) of Clouds A to E (from top to bottom). The gray shaded regions in the spectra indicate the velocity ranges that are used for the integration of each map. The gamma-ray emission of the first LHAASO catalogs is illustrated with cyan circles.

Table 2
Physical Parameters of Molecular Clouds in the J0341 Region

Cloud	ℓ (deg)	b (deg)	$V_{\rm LSR}$ (km s^{-1})	$\Delta V_{\rm LSR}$[a] (km s^{-1})	d (kpc)	Radius (pc)	$T_{\rm ex}$ (K)	$N(H_2)$[b] (10^{21} cm^{-2})	$M(H_2)$ ($M_\odot$)	$M_2(H_2)$[c] ($M_\odot$)	$n(H_2)$[d] (cm^{-3})
A	147.0	−1.74	1.33 ± 0.01	1.21 ± 0.02	<0.4	0.52	4.1 ± 3.9	0.28 ± 0.2	5.4 ± 3.6	⋯	370 ± 240
B	146.9	−1.46	4.94 ± 0.17	3.46 ± 0.41	<0.3	0.92	7.3 ± 4.0	1.2 ± 0.2	25 ± 4	⋯	310 ± 50
C	147.0	−1.51	−10.59 ± 0.01	1.85 ± 0.02	0.9 ± 0.4	1.6	10 ± 4	2.8 ± 0.2	310 ± 130	150 ± 70	780 ± 320
D	146.6	−2.06	−6.56 ± 0.06	3.87 ± 0.13	0.5 ± 0.4	0.99	4.5 ± 4.1	1.2 ± 0.2	21 ± 18	⋯	210 ± 170
E	147.2	−1.77	−39.88 ± 0.01	1.77 ± 0.03	4 ± 1	1.2	12 ± 4	3.6 ± 0.2	340 ± 90	130 ± 40	2100 ± 530

Notes.
[a] $\Delta V_{\rm LSR}$ indicates FWHM.
[b] $N(H_2)$ is averaged within the region.
[c] M_2 is a mass derived assuming LTE.
[d] n is derived assuming a sphere.

3.1. Physical Parameters of Molecular Clouds

In this subsection, we estimate physical parameters of the molecular clouds, including distance, column density, mass, and number density.

To estimate the distance to the clouds, we made use of a tool developed by T. V. Wenger et al. (2018).[11] Given the obtained locations and velocities of the molecular clouds, this tool calculates the traditional kinematic distance by using the Galactic rotation curves (e.g., J. Brand & L. Blitz 1993; M. J. Reid et al. 2014). It also calculates the Monte Carlo kinematic distance and its uncertainty from 10,000 Monte Carlo samples (T. V. Wenger et al. 2018). Since the direction to J0341 ($\ell = 146.^\circ7$) is near the Galactic anticenter and oriented toward the outer Solar circle (≈8 kpc from the Galactic center), the kinematic distance can be poorly constrained, particularly for positive and small values of $V_{\rm LSR}$. In Table 2, we show the distance derived by the Monte Carlo method (T. V. Wenger et al. 2018), because the traditional kinematic distance cannot be derived in the J0341 region for Clouds A and B.

The column density, $N(H_2)$, is estimated using two methods, as follows. The first method is to convert the ^{12}CO($J = 1$–0) integrated intensity to $N(H_2)$, assuming the X-factor of $X_{\rm CO} = 2 \times 10^{20}$ cm^{-2} (K km s^{-1})$^{-1}$. This factor has 10%–40% uncertainty at the Galactocentric radius of 8.5–12 kpc, which is derived for the position of the molecular clouds (N. Arimoto et al. 1996; A. D. Bolatto et al. 2013; S. Abe et al. 2024). The second one is to calculate the column density assuming local thermodynamic equilibrium (LTE). On the assumption that the ^{12}CO($J = 1$–0) line is optically thick, the excitation temperature ($T_{\rm ex}$) is derived from the ^{12}CO($J = 1$–0) data. With $T_{\rm ex}$ and the ^{12}CO($J = 1$–0) intensity, the ^{13}CO optical depth and column density, $N(^{13}$CO), can be calculated. Then, $N(^{13}$CO) is converted to $N(H_2)$ by multiplying by the ^{13}CO-to-H$_2$ factor of 7.7×10^5 (see, e.g., T. L. Wilson et al. 2009; E. de la Fuente et al. 2023; H. Sakemi et al. 2023 for details). It should be noted that the LTE method requires the use of the ^{13}CO($J = 1$–0) data to derive $N(^{13}$CO), therefore we applied it only to Clouds C and E, where the ^{13}CO($J = 1$–0) emission is clearly detected (Figures 3 and 4). The difference between the two methods is a factor of 2–3 (Table 2).

The mass, M, of the cloud can be derived by

$$M = 2\mu m_{\rm H} d^2 \Omega \sum_i [N_i(H_2)], \quad (1)$$

where μ (≈1.4) is the mean molecular weight, $m_{\rm H}$ is the mass of hydrogen, d is the distance, Ω is an angular area of a grid space (i.e., 7.5×7.5 arcsec^2), and i indicates each pixel. Table 2 summarizes the estimated mass, as well as a number density, n, derived by assuming a sphere. Note that the virial mass (G. Garay & S. Lizano 1999) is much larger than the estimated mass for all of the detected molecular clouds. In Table 2, the uncertainties of $V_{\rm LSR}$ and $\Delta V_{\rm LSR}$ are statistical ones when fitting the velocity spectra, that of the distance is taken from the estimation method of the Monte Carlo kinematic distance (T. V. Wenger et al. 2018), and those of N, M, and n arise from the rms. It should be noted that the systematic uncertainty on the velocity arises from its resolution, which is 1 km s^{-1} in our observations.

3.2. Summary

As summarized in Table 2, we find that most of the molecular clouds within the gamma-ray-emitting region are nearby ($d \lesssim 1$ kpc), relatively small ($\lesssim$ a few parsecs), and low in mass ($M \lesssim$ a few hundreds of solar masses). Descriptions of each cloud are provided below (see Appendix B for clouds outside the gamma-ray region):[12]

1. *Cloud A (half-shell).* As mentioned in Z. Cao et al. (2021b), a "half-shell" structure is located almost at the center of 1LHAASO J0343+5254u with WCDA (previously LHAASO J0341+5258 with KM2A). It is nearby ($d < 0.4$ kpc), and its mass is 5.4 $M_\odot$. Although the projected image looks like a half-shell, the position–velocity map does not show any hint of an expanding feature. Observations with better velocity resolution might be needed to confirm its property as an expanding shell.
2. *Clouds B and C (dense core).* Cloud C is detected in all ^{12}CO($J = 1$–0), ^{13}CO($J = 1$–0), and C^{18}O($J = 1$–0) lines, indicating it is a dense core of the cloud. Both Clouds B and C are distributed in two velocities of −10 km s^{-1} and 5 km s^{-1}. The association of these two clouds is not clear.

[11] https://github.com/tvwenger/kd

[12] The gamma-ray radius presented here indicates the 39% containment radius in the 2D Gaussian model. Thus, the molecular clouds outside r_{39} can potentially act as targets of proton–proton interactions. See also Figure 9 for the 68% containment radius overlying the molecular cloud map.

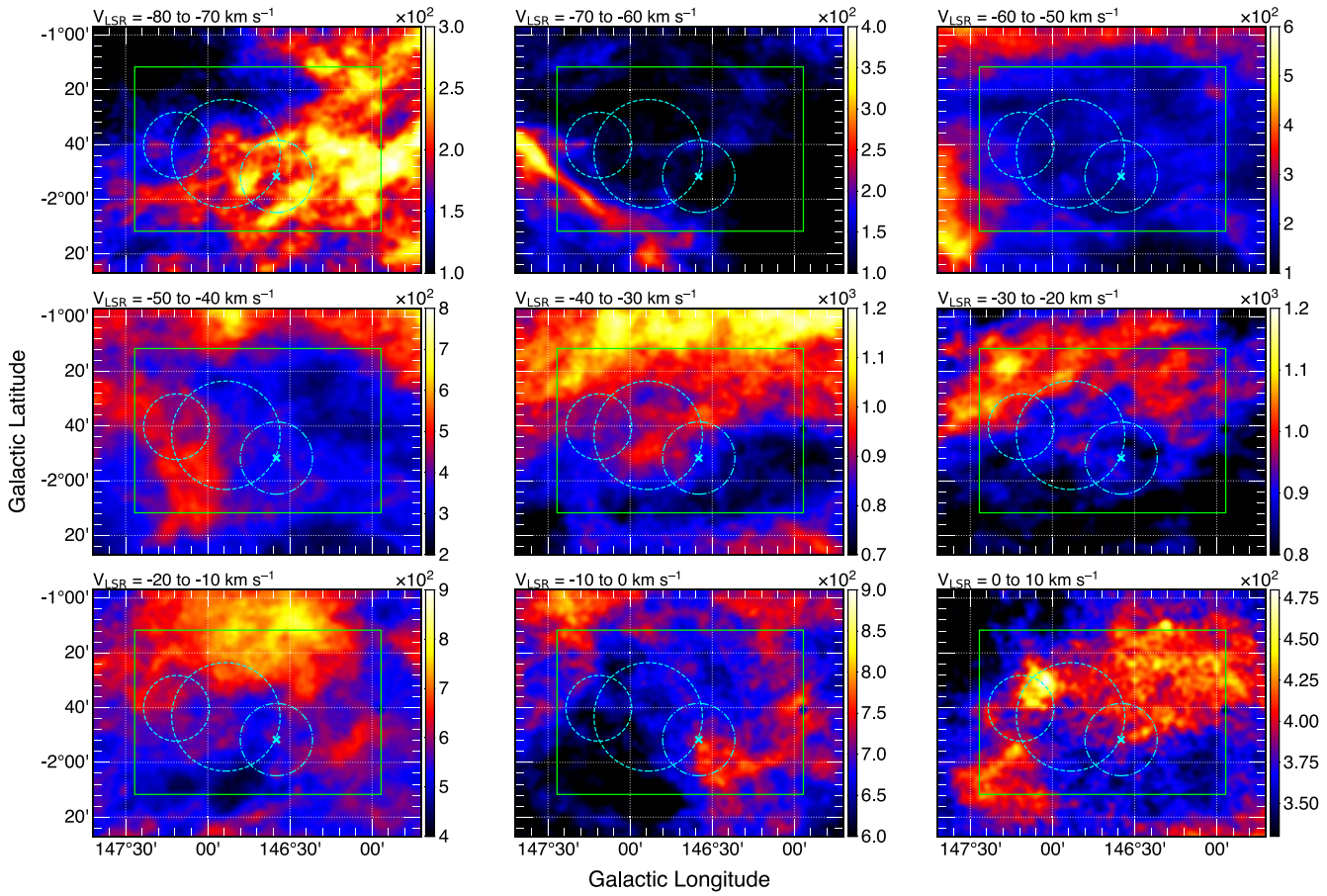

Figure 5. H I intensity maps at $V_{\rm LSR}$ of -80 to 10 km s^{-1} with a grid of 10 km s^{-1}, overlaid with the gamma-ray emission of the first LHAASO catalogs in cyan circles and the RoI in the green box. The intensity is shown in units of K km s^{-1}.

3. *Cloud D (filament-like).* This cloud is located near the outer edge of the gamma-ray source LHAASO J0339 +5307 with KM2A. The velocity width is relatively broad, $\Delta V \sim 4$ km s^{-1}, among the clouds in the J0341 region.
4. *Cloud E (point-like).* Cloud E has a compact, point-like structure, although it is extended compared to the angular resolution of 15″ of the NRO 45-m telescope. This source has optical and infrared counterparts, referred to as IRAS 03392+5239 (J. G. A. Wouterloot & J. Brand 1989). It is likely an evolved star, such as an asymptotic giant branch (AGB) star, surrounded by a CO envelope. However, the progenitor star of an AGB star has typically a mass of $\lesssim$10 $M_\odot$, which contradicts the obtained mass of 340 $M_\odot$ in Cloud E. The mass estimated by our CO data could be contaminated by CO gas that is not directly associated with the AGB star. High-resolution observations (e.g., by the Atacama Large Millimeter/submillimeter Array) may help clarify the association. Alternatively, Cloud E may represent a compact cloud clump or a core of molecular cloud (e.g., C. F. McKee & E. C. Ostriker 2007). The possibility of particle acceleration at Cloud E is discussed in Section 5.

4. H I and Continuum Observation

In addition to the CO data with the NRO 45-m telescope, we analyzed the archival data of the atomic hydrogen (H I) 21 cm line and continuum emission. These data were retrieved from the Canadian Galactic Plane Survey (CGPS).[13] We made use of the H I observations and continuum observations at 408 and 1420 MHz, covering the J0341 region, from the Dominion Radio Astrophysical Observatory archives (A. R. Taylor et al. 2003). These observations were performed in 2003–2004. The H I data have an angular resolution of 18″ and a velocity range from -165 to 59 km s^{-1} with a grid of 0.82 km s^{-1}. For the continuum radio data, the spatial resolution is 18″ at the 1420 MHz (Stokes I) band and 54″ at the 408 MHz band.

4.1. H I Cloud

In Figure 5, we show the H I map integrated in the velocity range from -80 to 10 km s^{-1} with a grid of 10 km s^{-1}. The H I emission is diffusively extended over our RoI, and there is no apparent counterpart of the gamma-ray emission observed by LHAASO and the molecular clouds by the NRO 45-m telescope. Assuming the H I-to-H conversion factor of 1.823×10^{18} cm^{-2} (K km s^{-1})$^{-1}$ (J. M. Dickey & F. J. Lockman 1990), we calculated the column density N(H I). Figure 6 compares the map and spectrum of H I with those of ^{12}CO($J=1$–0). Although the spectral shape is different between the H I and CO emission, we calculated the N(H I) (and mass, in turn) extracted from the same velocity range as that of CO. The proton column density, N(H) (and also the

[13] https://www.cadc-ccda.hia-iha.nrc-cnrc.gc.ca/en/search/

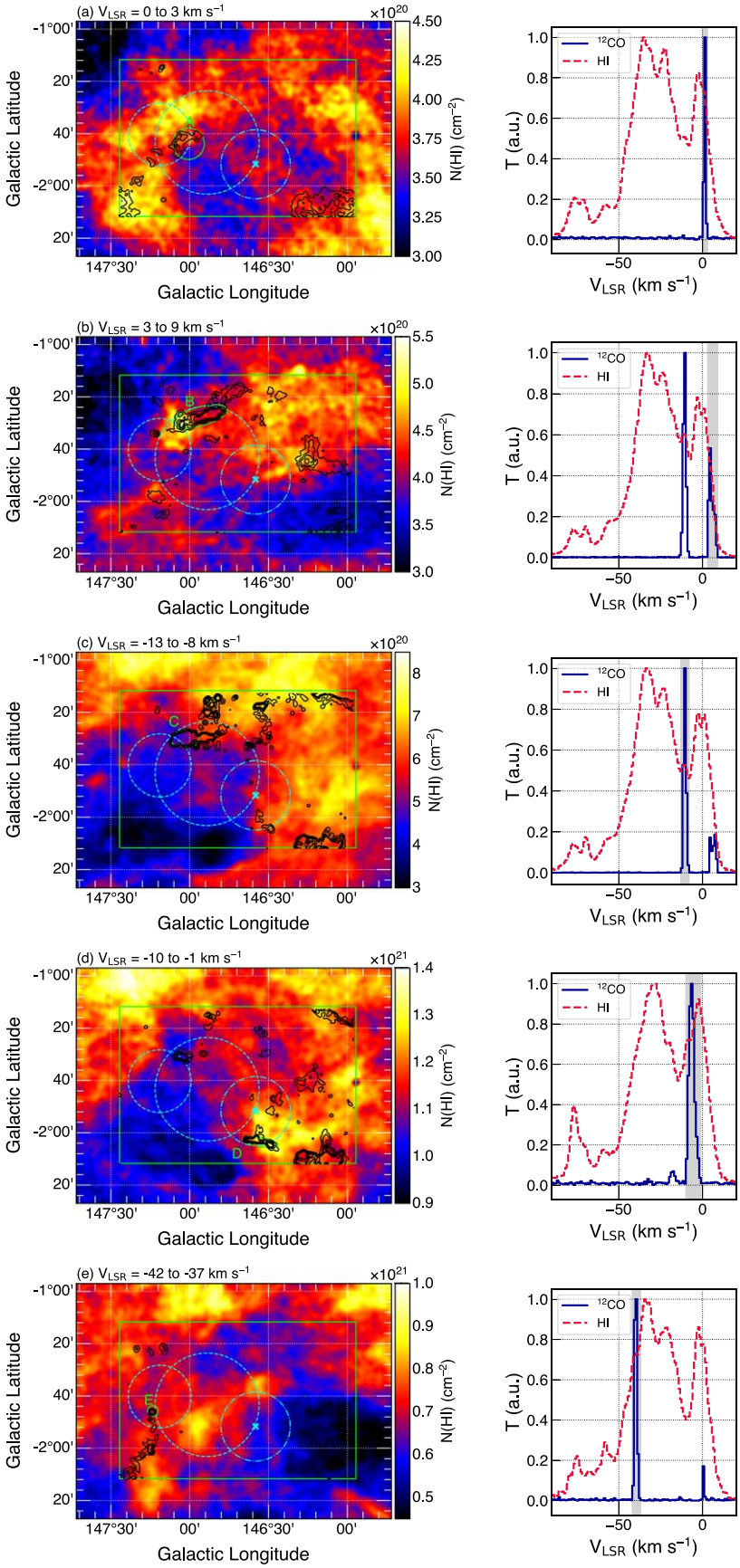

Figure 6. Left: H I map in the same velocity ranges of Clouds A–E, overlaid with the gamma-ray emission of the first LHAASO catalogs in cyan circles, the RoI in the green box, and the ^{12}CO($J = 1$–0) contour in black lines. Right: H I and ^{12}CO($J = 1$–0) spectra.

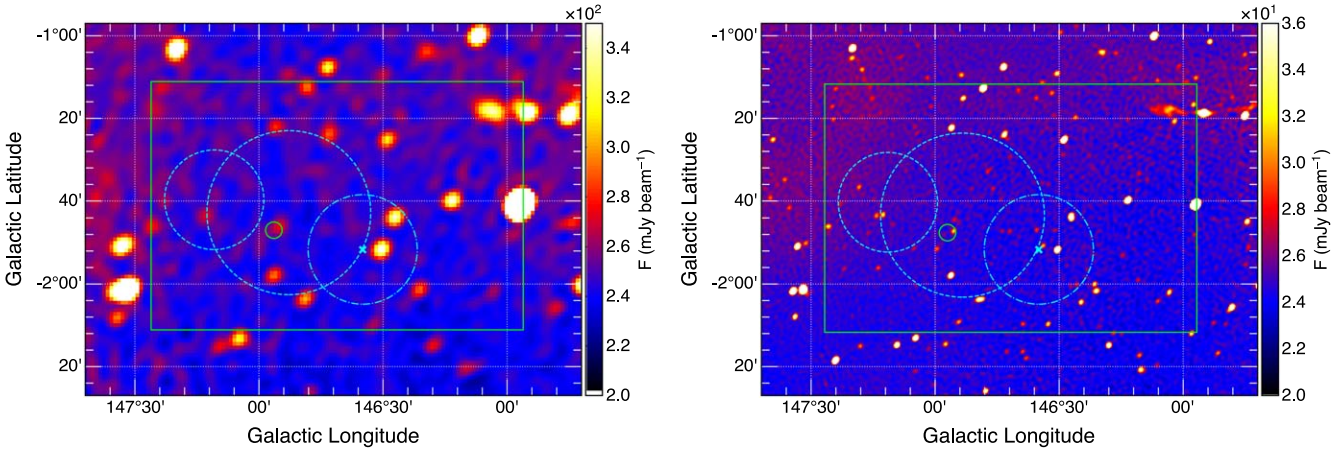

Figure 7. Radio continuum map at 408 MHz (left) and 1420 MHz (right), overlaid with the gamma-ray emission of the first LHAASO catalogs in cyan lines and the RoI in the green box. The green circle indicates the position of the X-ray extended source detected by XMM-Newton (S. DiKerby et al. 2025).

Table 3
Comparison of the CO and H I Clouds in J0341

Cloud	$N(H_2)$[a] (10^{21} cm^{-2})	N(H I)[a] (10^{21} cm^{-2})	$M(H_2)$ ($M_\odot$)	M(H I) ($M_\odot$)	$M(H_2 + H I)$ ($M_\odot$)	$n(H_2)$ (cm^{-3})	n(H I) (cm^{-3})	$n(H_2 + H I)$ (cm^{-3})
A	0.28 ± 0.20	0.37 ± 0.01	5.4 ± 3.6	7.2 ± 0.1	13 ± 4	370 ± 240	480 ± 8	1200 ± 480
B	1.2 ± 0.2	0.44 ± 0.01	25 ± 4	9.0 ± 0.1	34 ± 4	310 ± 50	110 ± 2	740 ± 100
C	2.8 ± 0.2	0.50 ± 0.01	310 ± 130	55 ± 22	360 ± 130	780 ± 320	140 ± 60	1700 ± 640
D	1.2 ± 0.2	1.40 ± 0.01	21 ± 18	23 ± 19	45 ± 26	210 ± 170	230 ± 180	650 ± 390
E	3.6 ± 0.2	0.59 ± 0.01	340 ± 90	56 ± 14	400 ± 88	2100 ± 530	350 ± 90	4500 ± 1100

Note.
[a] The column density, N, is the averaged value within the region, and the spatial grid size is 7.″5 and 18″ for the CO and H I data, respectively.

number density n(H)), is derived by

$$N(\mathrm{H}) = 2 \times N(\mathrm{H_2}) + N(\mathrm{H\,I}). \quad (2)$$

The total mass and number density of protons are summarized in Table 3.

If we derive the H I amount from the same region and velocity range as the CO data, the obtained mass and density are comparable to those of the molecular clouds in Clouds A and D and smaller in the rest (Table 3). The total proton number density, $n(H_2 + H I)$, is estimated to be $\sim 10^3$ cm^{-3}.

4.2. Continuum

Figure 7 shows the continuum maps at 408 MHz and 1420 MHz. The flux density, F, can be derived as

$$\left(\frac{F}{\mathrm{mJy\ \ beam^{-1}}}\right) = 8.2 \times 10^{-4}\left(\frac{T}{\mathrm{K}}\right)\left(\frac{\nu}{\mathrm{GHz}}\right)^2 \times \left(\frac{\theta_{\mathrm{major}} \times \theta_{\mathrm{minor}}}{\mathrm{arcsec^2}}\right), \quad (3)$$

where T and ν are the brightness temperature and frequency, respectively. A synthesized beam size ($\theta_{\mathrm{major}} \times \theta_{\mathrm{minor}}$) can be calculated as 2.′8 × 2.′8 × cosec δ at 408 MHz and 49″ × 49″ × cosec δ at 1420 MHz, where δ is the decl. (A. R. Taylor et al. 2003). With δ of 52.°97 in the J0341 region, the beam size is 2.′8 × 3.′5 and 49″ × 61″ at 408 MHz and 1420 MHz, respectively. The rms noise level is 3.8 (408 MHz) and 0.27 (1420 MHz) mJy beam^{-1} (A. R. Taylor et al. 2003). There is no diffuse emission corresponding to the gamma rays but there are some point-like sources. Table 4 shows the radio continuum flux, extracted from the gamma-ray-emitting regions detected by LHAASO. Since the background is not taken into account, the flux should be considered an upper limit. Note that excluding the point-like sources does not largely affect the obtained flux.

Table 4
Radio Continuum Flux in J0341

Name	Instrument	$F_{408\ \mathrm{MHz}}$ (erg cm^{-2} s^{-1})	$F_{1420\ \mathrm{MHz}}$ (erg cm^{-2} s^{-1})
1LHAASO J0339+5307	LHAASO KM2A	5.6×10^{-14}	2.3×10^{-13}
1LHAASO J0343 +5254u	LHAASO KM2A	4.6×10^{-14}	2.0×10^{-13}
1LHAASO J0343 +5254u	LHAASO WCDA	1.3×10^{-13}	5.2×10^{-13}
1LHAASO total[a]	…	2.0×10^{-13}	8.2×10^{-13}
New extended X-ray	XMM-Newton	1.2×10^{-15}	4.3×10^{-15}

Note.
[a] 1LHAASO J0339+5307 and 1LHAASO J0343+5254u are merged.

5. Discussion

Figure 8 shows the known counterparts within the RoI, including a pulsar (PSR J0343+5312), an unidentified Fermi Large Area Telescope GeV gamma-ray source (4FGL J0340.4 +5302), and ROSAT X-ray sources from the 2RXS catalog. PSR J0343+5312 is unlikely to be relevant to the UHE

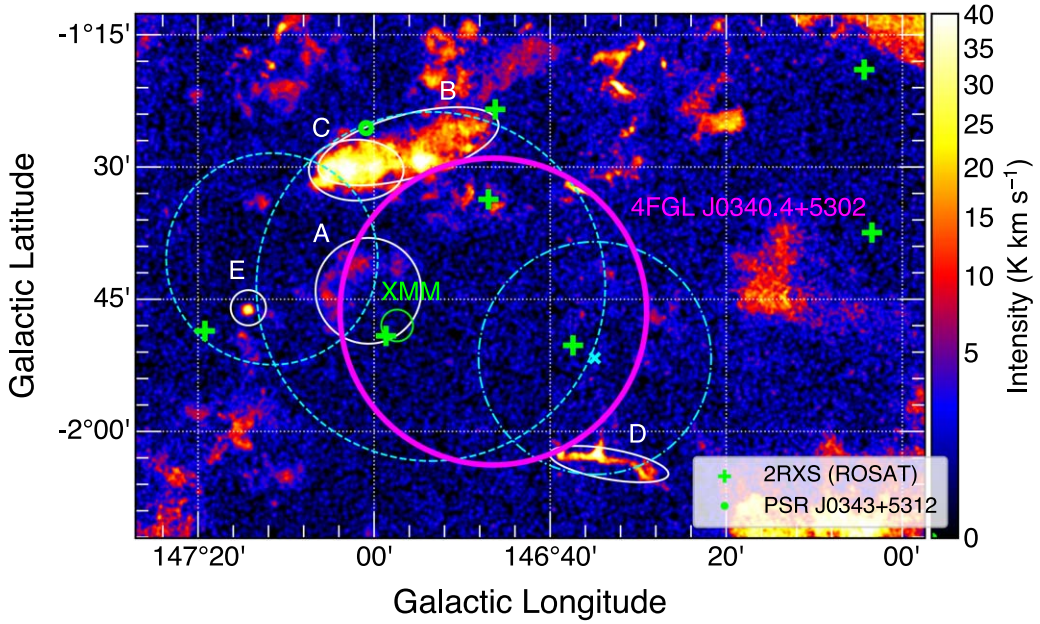

Figure 8. The ^{12}CO($J = 1$–0) map with $V_{\rm LSR} = -40$ to 10 km s^{-1}, overlaid with the gamma-ray emission of the first LHAASO catalogs (cyan circles), a known counterpart of PSR J0343+5312 (the green small circle), 4FGL J0340.4+5302 (the magenta circle), ROSAT sources from the 2RXS catalog (green crosses), and a newly detected XMM-Newton source (the green circle; S. DiKerby et al. 2025). Clouds A–E are marked in white.

gamma-ray emission, given its low power of $\sim 10^{31}$ erg s^{-1}. We also show the position of a newly detected XMM-Newton source, which is likely a pulsar wind nebula (PWN; S. DiKerby et al. 2025). The new XMM-Newton source is located near Cloud A, thus if they are associated with each other, the X-ray source could be at less than 0.4 kpc. The flux of the radio continuum emission from this X-ray source is $\lesssim 10^{-15}$ erg cm^{-2} s^{-1} (Table 4). It should be noted that the ROSAT point source (2RXS J034125.8+525530), located near the edge of Cloud A and the XMM-Newton extended source, did not appear in the new XMM-Newton data (S. DiKerby et al. 2025), suggesting that it is a transient source and not related to the extended emission. The PWN scenario, including detailed leptonic spectral energy distribution modeling, is presented in a separate publication (S. DiKerby et al. 2025).

If the gamma-ray emission is hadronic, a total proton energy (W_p) can be calculated as $W_p = 4\pi d^2 F_\gamma t_{\pi^0} \eta^{-1}$, where F_γ, t_{π^0} ($\approx 1.5 \times 10^{15} n^{-1}$ s), and η (≈ 1.5–2) denote the gamma-ray flux, a timescale of proton–proton interactions, and a parameter to take into account the gamma-ray production in interactions involving the nuclei of both CRs and the interstellar medium (E. Kafexhiu et al. 2014), respectively. Adopting the gamma-ray flux of 2.4×10^{-12} erg cm^{-2} s^{-1} (Z. Cao et al. 2024a),

$$W_p(E > 1\ \mathrm{TeV}) \sim 3 \times 10^{45} \times \left(\frac{d}{1\ \mathrm{kpc}}\right)^2 \left(\frac{n}{100\ \mathrm{cm^{-3}}}\right)^{-1} \mathrm{erg}. \quad (4)$$

Note that the proton spectrum was obtained to be a cutoff power-law model with an index of $\leqslant 2$ and a cutoff energy of 200–300 TeV in the hadronic case (Z. Cao et al. 2021b; A. Kar & N. Gupta 2022; A. De Sarkar & P. Majumdar 2024). Although the molecular clouds detected by the NRO 45-m telescope (Clouds A–E) do not have exact counterparts of the known sources, the observations provide important parameters, such as the distance and number density. Some of the known sources and the gamma-ray emission may be located at the same distance as Clouds A–E. If so, the distance would be $\lesssim 1$ kpc or ~ 4 kpc. The total number density of protons in Clouds A–E is $n \sim 700$–5000 cm^{-3} (Table 3). Thus, the proton energy could be $\lesssim 10^{45}$ erg, inferred from Equation (4). This is much smaller than the typical SNR value, where the explosion energy is $\sim 10^{51}$ erg and the conversion efficiency from the explosion energy to CR acceleration is $\sim 1\%$–10%. If the gamma-ray radiation is of hadronic origin, it might originate from molecular clouds illuminated by escaping CRs, rather than any hadronic acceleration site. The narrow velocity width of 1–4 km s^{-1} of the detected clouds may also support the idea that dynamical power, which could be expected for CR accelerators such SNRs, is not injected. Further observations with a better velocity resolution and/or other transition line emissions would be helpful. As inferred from our analysis, the distances to most of the clouds could be smaller than 1 kpc, and thus there may exist hadronic accelerators outside our RoI in this paper. In the vicinity of J0341, there are roughly 10 SNRs within 20° (G. Ferrand & S. Safi-Harb 2012). This corresponds to <360 pc for $d < 1$ kpc and <1.2 kyr for protons to travel, which is consistent with the assumptions in A. M. W. Mitchell et al. (2021). We find that three of them (G156.2+05.7, G160.9+02.6, and G166.0+04.3) might have potential contribution to the J0341 region, because they are relatively young, shell-like, and likely detected in the GeV gamma-ray band.

In this paper, we study the distribution of CO and H I to investigate the gas in the gamma-ray-emitting region. Additionally, there exists the so-called "dark gas," which cannot be traced by the CO and H I line emissions. It has been shown that the amount of the dark gas would be likely ~ 0.1–5 times that of H_2 and H I, depending on the total mass (e.g., I. A. Grenier et al. 2005, 2015; T. Mizuno et al. 2022). The detection of several molecular clouds by the the NRO 45-m telescope suggests that these clouds, which may be surrounded by the

dark gas, could be potential target gas for producing hadronic gamma rays, even though their angular sizes are smaller than those of the gamma-ray emission. Taking into account the dark cloud, the total mass and number density might be several times larger, and thus W_p may become smaller than 10^{45} erg in the hadronic scenario.

Cloud E, which is likely a CO envelope of an AGB star (IRAS 03392+5239; J. G. A. Wouterloot & J. Brand 1989), is located at nearly the center of 1LHAASO J0343+5254 (KM2A), as shown in the bottom panel of Figure 4. Remarkably, there is a tail-like structure that is likely launched from the compact CO object and that might be a bow shock (e.g., N. L. J. Cox et al. 2012). Although the association of Cloud E with the AGB star is unclear, as mentioned in Section 3.2, we now explore the possibility of particle acceleration at AGB stars to test whether Cloud E itself can act as a CR accelerator. Since the size (D) of Cloud E is 2′ in diameter, corresponding to 2.3 pc at $d = 4$ kpc, and the velocity width (ΔV) is 1.8 km s^{-1} (Table 2), a dynamical time can be estimated as $t_{\rm dyn} = D/\Delta V = 1.3$ Myr. Given its mass of 340 $M_\odot$ (Table 2), a mass-loss rate is calculated as $\dot{M} = M/t_{\rm dyn} = 2.6 \times 10^{-4}\,M_\odot\,{\rm yr}^{-1}$. Applying the same calculation to the tail-like structure, we obtain a size of 20 pc, a mass of 950 $M_\odot$, a dynamical timescale of 11 Myr, and a mass-loss rate of $7.3 \times 10^{-4}\,M_\odot\,{\rm yr}^{-1}$. Particle acceleration at stellar winds has been discussed in, e.g., G. Morlino et al. (2021) and P. Blasi & G. Morlino (2023). The maximum attainable energy depends on various conditions, and one example is provided as

$$E_{\rm max} = 90\left(\frac{L_c}{2\ {\rm pc}}\right)^{-1}\left(\frac{\eta_B}{0.1}\right)^{\frac{1}{2}}\left(\frac{\dot{M}}{10^{-4}\,M_\odot\ {\rm yr}^{-1}}\right)^{\frac{1}{5}}\left(\frac{v}{2\ {\rm km\ \ s}^{-1}}\right)^{\frac{2}{5}} \times \left(\frac{n}{1000\ {\rm cm}^{-3}}\right)^{\frac{3}{10}}\left(\frac{t}{1\ {\rm Myr}}\right)^{-\frac{2}{5}}\ {\rm TeV}, \quad (5)$$

adjusted from Equation (18) in P. Blasi & G. Morlino (2023). This assumes that the scattering occurs in the inertial range of a Kraichnan-like turbulence. η_B is a fractional ratio of the wind's kinetic energy transferred to the magnetic field. Adopting the obtained parameters of Cloud E and $\eta_B = 0.1$, Equation (5) yields a maximum energy of $\sim$90 TeV. Although the mass-loss rate of Cloud E and the tail-like structure ($\sim 10^{-4}$–$10^{-3}\,M_\odot\,{\rm yr}^{-1}$) is relatively high, the velocity is as low as 2 km s^{-1}, resulting in the low maximum energy. It should be noted that under different conditions (e.g., different turbulences, such as Equations (13) and (16) in G. Morlino et al. 2021, where $E_{\rm max}$ is more dependent on the wind velocity), the estimated maximum energy became much smaller than 90 TeV. To conclude, it might be challenging for the AGB star (Cloud E) to accelerate particles beyond 100 TeV and to reconcile with the detection of >100 TeV gamma rays at 1LHAASO J0343+5254u with KM2A. Nevertheless, it would be worth theoretically and observationally investigating the possibility of efficient particle acceleration at AGB stars, which may emerge as a new class of CR accelerators.

As the new extended X-ray source has been detected in 1LHAASO J0343+5254u (WCDA; S. DiKerby et al. 2025), follow-up X-ray observations are needed for the other gamma-ray regions, 1LHAASO J0343+5254u (KM2A) and 1LHAASO J0339+5307 (KM2A), to explore and understand the nature of the J0341 complex. High-resolution and wide-field-of-view X-ray observations, such as with AXIS[14] (C. S. Reynolds et al. 2023; S. Safi-Harb et al. 2023), would be useful. Further gamma-ray observations using Imaging Atmospheric Cherenkov Telescopes (IACTs) with better angular resolution would also help reveal a detailed gamma-ray structure and identify the accelerator. If the hadronic scenario is established, accompanying neutrinos can be tested by searching for them with next-generation observatories (e.g., S. Aiello et al. 2019; B. Clark 2021).

6. Conclusions

J0341, discovered by LHAASO, is an unidentified, extended source, detected even at >100 TeV, making it one of the Galactic PeVatron candidate sources. In order to reveal its nature, we have conducted molecular line observations with the NRO 45-m radio telescope. Within the gamma-ray-emitting region, we have detected five sources, Clouds A–E. Clouds A–D are relatively nearby ($d \lesssim 1$ kpc), compact (with radii of 0.5–1.6 pc), light ($M \sim 5$–$300\ M_\odot$), and dense ($n \sim 200$–800 cm^{-3}). Cloud E, a compact emission with optical and infrared counterparts IRAS 03392+5239, likely represents a CO envelope of an AGB star or a compact cloud clump. We have demonstrated that Cloud E might not be able to accelerate particles up to the PeV range. We have also analyzed archival CGPS radio data. The H I clouds are extended and have comparable or lower mass than the CO clouds. If the CO and H I data are combined, the total proton number density is 700–5000 cm^{-3}. In the 408 and 1420 MHz bands, there are only point-like sources and no apparent counterparts of the gamma rays in our RoI, and we derived flux upper limits of $\sim 10^{-13}$ erg cm^{-2} s^{-1}. If the gamma rays are of hadronic origin (i.e., associated with the detected molecular clouds), our findings indicate that the total proton budget is $\sim 10^{45}$ erg. This is relatively small, suggesting that the gamma-ray emission might originate from molecular clouds illuminated by escaping CRs (CR–cloud interaction), rather than accelerators (such as SNR–cloud interaction). Combined with follow-up X-ray observations (e.g., S. DiKerby et al. 2025) and gamma-ray observations with IACTs, the origin of the gamma-ray radiation will be unveiled.

Acknowledgments

We are grateful to the anonymous referee for the helpful comments. We thank Hidetoshi Sano, Tsunefumi Mizuno, and Laura Olivera-Nieto for the fruitful discussion. We also thank Fiorenza Donato, Charles Hailey, Mattia Di Mauro, and Siliva Manconi for the preparation of the proposals. We are grateful to the staff of the Nobeyama Radio Observatory (NRO) for their outstanding support during the 45-m telescope observations. The NRO is a branch of the National Astronomical Observatory of Japan (NAOJ), National Institutes of Natural Sciences. This work was supported by the Japan Society for the Promotion of Science (JSPS) KAKENHI grant Nos. JP22K14064 and JP24H01819 (N.T.). This research has been partly supported by a grant from the Research Institute for Integrated Science, Kanagawa University (RIIS202403). Support for K.M. and J.W. was provided by NASA through the XMMNC22 grant. S.S.H. acknowledges support by the Natural Sciences and Engineering Research Council of Canada

[14] https://blog.umd.edu/axis/

(NSERC) through the Canada Research Chairs and Discovery Grants programs, and by the Canadian Space Agency.

Facility: NRO.

Appendix A
Supplementary Figures

We show ^{12}CO($J = 1$–0) maps at different velocity ranges in Figure 9 and the velocity spectrum from the entire RoI in Figure 10.

Appendix B
Molecular Clouds Outside the Gamma-Ray Region

Here, we present molecular clouds detected outside LHAASO's gamma-ray extent (Figure 11 and Table 5). It should be noted that the gamma-ray extension in this paper (Table 1) indicates the 39% containment radius assuming the 2D Gaussian model (see Figure 9 for the 68% containment radius). Therefore, the clouds outside this radius might also be associated with gamma rays.

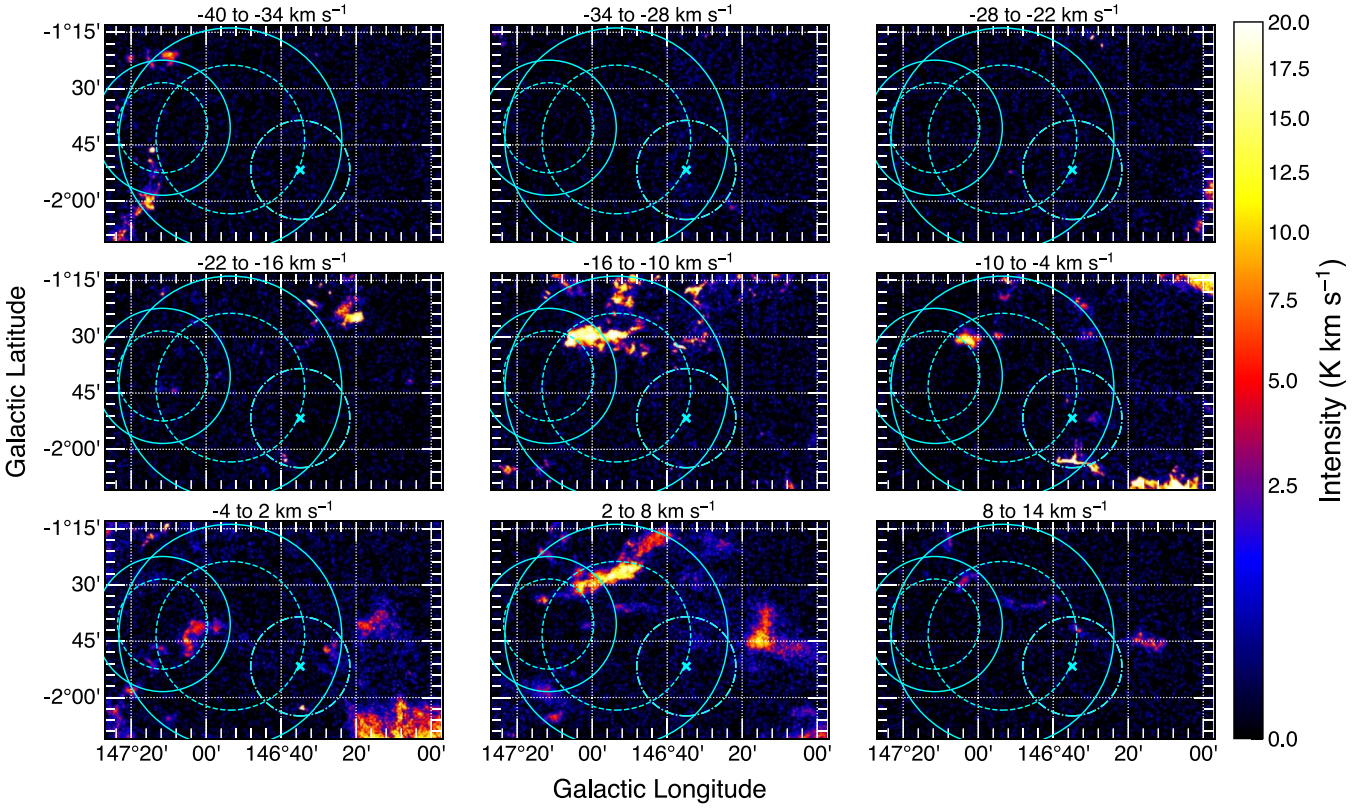

Figure 9. ^{12}CO($J = 1$–0) maps at different velocities with the interval of 6 km s^{-1} from -40 to 14 km s^{-1}. The dashed and solid circles indicate the radii of 39% and 68% containment of 1LHAASO J0343+5254u, respectively (Z. Cao et al. 2024a). For 1LHAASO J0339+5307, the position and 95% upper limit of the radius are shown with the cyan cross and dashed–dotted circle, respectively.

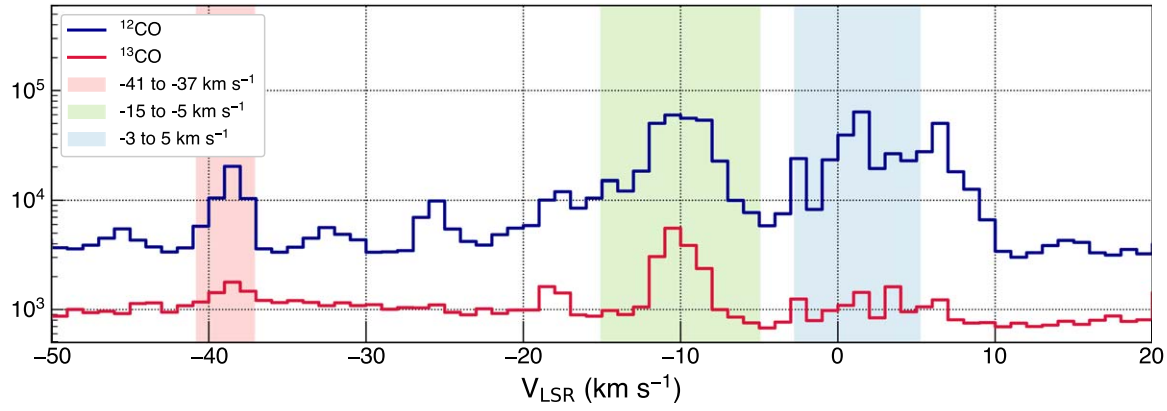

Figure 10. ^{12}CO($J = 1$–0) and ^{13}CO($J = 1$–0) velocity distributions extracted from the entire RoI.

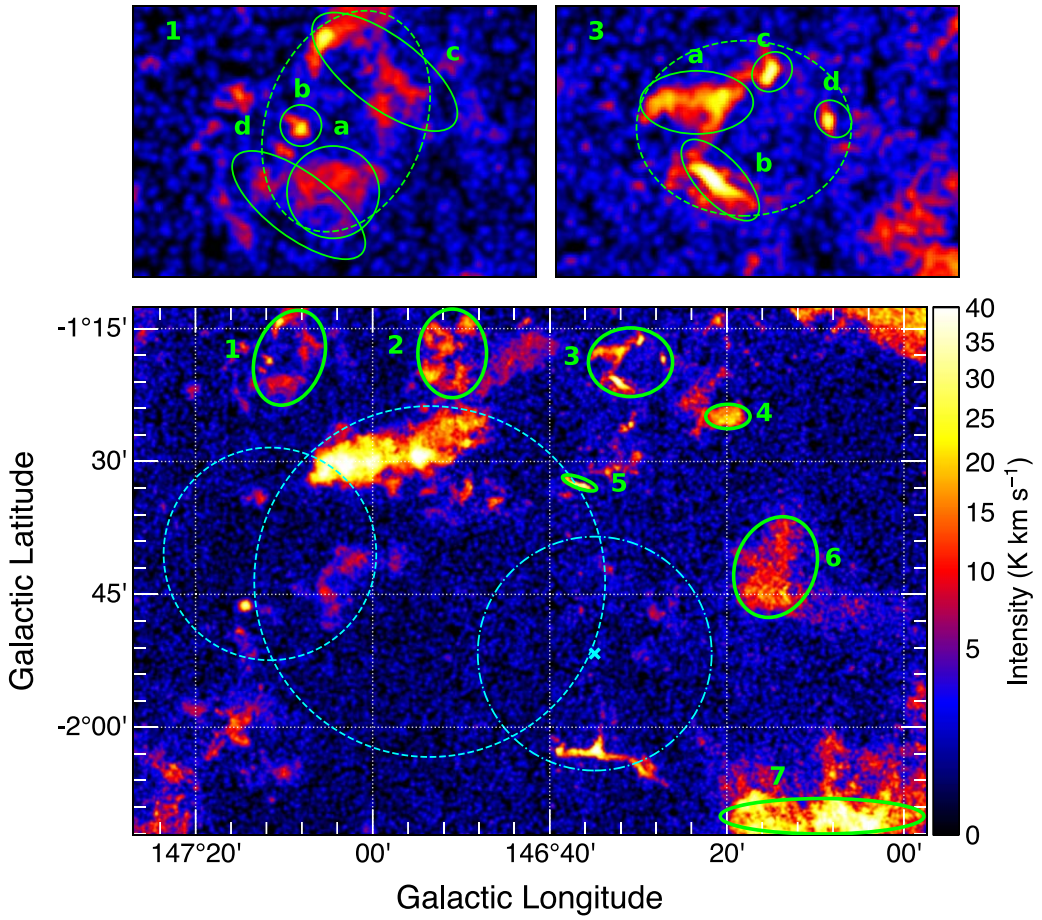

Figure 11. ^{12}CO($J = 1$–0) map integrated over −40 to 10 km s^{-1}, shown with labels of the clouds outside the gamma-ray extent. The upper left and right panels illustrate the zoom-in images of Clouds 1 and 3, respectively.

Table 5
Physical Parameters of Clouds Outside the J0341 Region

Cloud	ℓ (deg)	b (deg)	V_{LSR} (km s^{-1})	ΔV_{LSR} (km s^{-1})	d (kpc)	R_{min}[a] (pc)	R_{maj}[a] (pc)	T_{ex} (K)	$N(H_2)$ (10^{21} cm^{-2})	$M(H_2)$ ($M_\odot$)	$n(H_2)$[b] (cm^{-3})
1a	147.2	−1.36	−37.98 ± 0.00	1.07 ± 0.05	3.7 ± 0.9	2.4	2.4	5.1 ± 3.9	0.37 ± 0.18	150 ± 83	104 ± 59
1b	147.2	−1.31	−15.69 ± 0.18	4.35 ± 0.33	1.5 ± 0.8	0.37	0.37	4.1 ± 3.9	0.98 ± 0.18	9.4 ± 5.4	1800 ± 1100
1c	147.1	−1.27	−14.98 ± 0.00	1.23 ± 0.04	1.2 ± 0.5	0.68	1.7	4.3 ± 3.8	0.48 ± 0.18	38 ± 22	1200 ± 660
1d	147.2	−1.37	7.47 ± 0.02	0.99 ± 0.02	<0.2	0.077	0.19	4.4 ± 3.9	0.28 ± 0.18	0.29 ± 0.19	6200 ± 4100
2	146.9	−1.30	−10.95 ± 0.03	1.97 ± 0.09	0.73 ± 0.6	1	1.3	5.4 ± 4.2	1.1 ± 0.24	100 ± 52	960 ± 500
3a	146.6	−1.30	−11.34 ± 0.01	1.46 ± 0.01	0.87 ± 0.5	0.39	0.71	8.4 ± 4.1	1.6 ± 0.22	32 ± 18	5100 ± 2800
3b	146.5	−1.35	−17.06 ± 0.07	3.72 ± 0.19	1.5 ± 0.7	0.43	0.98	5.1 ± 3.9	1.5 ± 0.19	45 ± 20	5400 ± 2400
3c	146.5	−1.27	−22.70 ± 0.20	3.37 ± 0.50	2.1 ± 0.8	0.49	0.57	4.8 ± 3.9	1.2 ± 0.19	24 ± 9	2000 ± 780
3d	146.5	−1.31	−22.22 ± 0.14	3.86 ± 0.38	1.9 ± 0.7	0.44	0.54	4.4 ± 4.1	1.1 ± 0.21	18 ± 7.2	2000 ± 800
4	146.3	−1.42	−17.91 ± 0.01	1.82 ± 0.04	1.4 ± 0.7	0.57	1	9 ± 4.2	2.5 ± 0.24	110 ± 48	5500 ± 2500
5	146.6	−1.54	−13.73 ± 0.02	2.88 ± 0.05	1.1 ± 0.7	0.23	0.75	7.3 ± 4.3	2.4 ± 0.26	30 ± 14	25,000 ± 12,000
6	146.2	−1.70	6.24 ± 0.33	0.93 ± 0.65	<0.24	0.32	0.41	6.5 ± 4.3	0.97 ± 0.26	8.8 ± 2.4	2700 ± 730
7	146.2	−2.17	−8.81 ± 0.02	1.76 ± 0.05	0.69 ± 0.4	0.37	2.1	8.5 ± 4.3	1.9 ± 0.26	110 ± 78	20,000 ± 15,000

Notes.
[a] R_{min} and R_{maj} indicate minor-axis and major-axis radii, respectively.
[b] n is derived by assuming a sphere and using the minor-axis radius.

ORCID iDs

Naomi Tsuji https://orcid.org/0000-0001-7209-9204
Shunya Takekawa https://orcid.org/0000-0001-8147-6817
Kaya Mori https://orcid.org/0000-0002-9709-5389
Alison Mitchell https://orcid.org/0000-0003-3631-5648
Shuo Zhang https://orcid.org/0000-0002-2967-790X
Priyadarshini Bangale https://orcid.org/0000-0002-3886-3739
Stephen DiKerby https://orcid.org/0000-0003-2633-2196
Tülün Ergin https://orcid.org/0000-0003-2423-4656
Jooyun Woo https://orcid.org/0009-0001-6471-1405
Samar Safi-Harb https://orcid.org/0000-0001-6189-7665
Shinta Kasuya https://orcid.org/0009-0004-4904-5792

References

Abdollahi, S., Acero, F., Ackermann, M., et al. 2020, ApJS, 247, 33
Abe, S., Abhir, J., Abhishek, A., et al. 2024, JCAP, 2024, 081
Abeysekara, A. U., Archer, A., Benbow, W., et al. 2020, ApJ, 894, 51
Ackermann, M., Ajello, M., Allafort, A., et al. 2013, Sci, 339, 807
Aharonian, F., Ashkar, H., Backes, M., et al. 2022, A&A, 666, A124
Aharonian, F. A. 2013, APh, 43, 71
Aiello, S., Akrame, S. E., Ameli, F., et al. 2019, APh, 111, 100
Alfaro, R., Alvarez, C., Arteaga-Velázquez, J. C., et al. 2024, Natur, 634, 557
Amenomori, M., Ayabe, S., Chen, D., et al. 2005, ApJ, 633, 1005
Arimoto, N., Sofue, Y., & Tsujimoto, T. 1996, PASJ, 48, 275
Bangale, P., & Wang, X. 2023, ICRC (Nagoya), 38, 0706
Blasi, P., & Morlino, G. 2023, MNRAS, 523, 4015
Bolatto, A. D., Wolfire, M., & Leroy, A. K. 2013, ARA&A, 51, 207
Brand, J., & Blitz, L. 1993, A&A, 275, 67
Cao, Z., Aharonian, F. A., An, Q., et al. 2021a, Natur, 594, 33
Cao, Z., Aharonian, F., An, Q., et al. 2021b, ApJL, 917, L4
Cao, Z., Aharonian, F., An, Q., et al. 2024a, ApJS, 271, 25
Cao, Z., Aharonian, F., Axikegu, et al. 2024b, SciBu, 69, 2833
Clark, B. 2021, JInst, 16, C10007
Cox, N. L. J., Kerschbaum, F., van Marle, A. J., et al. 2012, A&A, 537, A35
Dame, T. M., Hartmann, D., & Thaddeus, P. 2001, ApJ, 547, 792
Dame, T. M., & Thaddeus, P. 2022, ApJS, 262, 5
de la Fuente, E., Toledano-Juarez, I., Kawata, K., et al. 2023, PASJ, 75, 546
De Sarkar, A., & Majumdar, P. 2024, A&A, 681, A34
Dickey, J. M., & Lockman, F. J. 1990, ARA&A, 28, 215
DiKerby, S., Zhang, S., Ergin, T., et al. 2025, ApJ, 983, 21
Ferrand, G., & Safi-Harb, S. 2012, AdSpR, 49, 1313
Funk, S. 2015, ARNPS, 65, 245
Garay, G., & Lizano, S. 1999, PASP, 111, 1049
Giunti, L., Acero, F., Khélifi, B., et al. 2022, A&A, 667, A130
Grenier, I. A., Black, J. H., & Strong, A. W. 2015, ARA&A, 53, 199
Grenier, I. A., Casandjian, J.-M., & Terrier, R. 2005, Sci, 307, 1292
HAWC Collaboration, Abeysekara, A., Albert, A., et al. 2020, PhRvL, 124, 021102
H.E.S.S. Collaboration 2024, Sci, 383, 402
H.E.S.S. Collaboration, Abdalla, H., Abramowski, A., et al. 2018, A&A, 612, A3
Kafexhiu, E., Aharonian, F., Taylor, A. M., & Vila, G. S. 2014, PhRvD, 90, 123014
Kar, A., & Gupta, N. 2022, ApJ, 926, 110
Kuno, N., Takano, S., Iono, D., et al. 2011, in 2011 XXXth URSI General Assembly and Scientific Symp. (Piscataway, NJ: IEEE), 1
Kutner, M. L., & Ulich, B. L. 1981, ApJ, 250, 341
LHAASO Collaboration 2010, ChPhC, 34, 249
LHAASO Collaboration 2024a, SciBu, 69, 449
LHAASO Collaboration 2024b, arXiv:2410.08988
McKee, C. F., & Ostriker, E. C. 2007, ARA&A, 45, 565
Minamidani, T., Nishimura, A., Miyamoto, Y., et al. 2016, Proc. SPIE, 9914, 99141Z
Mitchell, A. M. W., Rowell, G. P., Celli, S., & Einecke, S. 2021, MNRAS, 503, 3522
Mizuno, T., Hayashi, K., Metzger, J., et al. 2022, ApJ, 935, 97
Morlino, G., Blasi, P., Peretti, E., & Cristofari, P. 2021, MNRAS, 504, 6096
Reid, M. J., Menten, K. M., Brunthaler, A., et al. 2014, ApJ, 783, 130
Reynolds, C. S., Kara, E. A., Mushotzky, R. F., et al. 2023, Proc. SPIE, 12678, 126781E
Safi-Harb, S., Burdge, K. B., Bodaghee, A., et al. 2023, arXiv:2311.07673
Sakemi, H., Machida, M., Yamamoto, H., & Tachihara, K. 2023, PASJ, 75, 338
Sawada, T., Ikeda, N., Sunada, K., et al. 2008, PASJ, 60, 445
Tanaka, T., Uchiyama, Y., Aharonian, F. A., et al. 2008, ApJ, 685, 988
Taylor, A. R., Gibson, S. J., Peracaula, M., et al. 2003, AJ, 125, 3145
Tsuji, N., Tanaka, T., Safi-Harb, S., et al. 2024, ApJ, 967, 138
Tsuji, N., Uchiyama, Y., Khangulyan, D., & Aharonian, F. 2021, ApJ, 907, 117
Wenger, T. V., Balser, D. S., Anderson, L. D., & Bania, T. M. 2018, ApJ, 856, 52
Wilson, T. L., Rohlfs, K., & Hüttemeister, S. 2009, Tools of Radio Astronomy (Berlin: Springer)
Wouterloot, J. G. A., & Brand, J. 1989, A&AS, 80, 149